

Finite-length effects and Coulomb interaction in Josephson junctions based on Ge quantum wells and probed with microwave spectroscopy


S.C. ten Kate,¹ D.C. Ohnmacht², M. Coraiola,¹ T. Antonelli,¹ S. Paredes¹, F.J. Schupp,¹ M. Hinderling,¹ S.W. Bedell³, W. Belzig², J.C. Cuevas⁴, A.E. Svetogorov², F. Nichele^{1,*}, and D. Sabonis^{1,†}

¹*IBM Research Europe - Zurich, Säumerstrasse 4, 8803 Rüschlikon, Switzerland*

²*Fachbereich Physik, Universität Konstanz, D-78457 Konstanz, Germany*

³*IBM Quantum, T.J. Watson Research Center, 1101 Kitchawan Road, Yorktown Heights, New York 10598, USA*

⁴*Departamento de Física Teórica de la Materia Condensada and Condensed Matter Physics Center (IFIMAC), Universidad Autónoma de Madrid, E-28049 Madrid, Spain*

 (Received 8 August 2025; revised 31 October 2025; accepted 4 November 2025; published 1 December 2025)

Proximitized Ge quantum wells have emerged as a platform for studying Andreev bound states (ABSs) due to their expected strong spin-orbit interaction and high mobility. Here, we used microwave spectroscopy techniques to investigate ABSs in Josephson junctions (JJs) realized in proximitized Ge quantum wells. Spectroscopic signatures observed in a 350-nm junction indicated the presence of multiple ABSs and were reproduced with a model including finite-length effects. The ABS spectra measured for a 1.2- μm junction were explained by a model including three ABSs in two conduction channels and finite Coulomb interaction. Our work highlights the importance of interactions in JJs and serves as a basis for understanding and manipulating ABSs in Ge-based hybrid devices.

DOI: [10.1103/hb1h-8jn9](https://doi.org/10.1103/hb1h-8jn9)

I. INTRODUCTION

A semiconductor confined between two superconductors forms a Josephson junction (JJ), where discrete subgap states, known as Andreev bound states (ABSs) arise, which are responsible for the current transport across the JJ [1–4]. These states have been successfully probed using spectroscopy techniques in dc transport [5–7] and microwave-domain [8–20] experiments, where the effects of Coulomb [14,16,21,22], exchange [18], and spin-orbit [10–12,14,15,18,20] interactions have been demonstrated for InAs-nanowire-based junctions. Recently, a hard induced superconducting gap has been demonstrated in Ge quantum wells [23], forming a platform for studying ABSs. It has been shown that the two-dimensional hole gases formed in these quantum wells have high mobility [24] and strong spin-orbit interaction [25]. Moreover, isotopic purification provides the opportunity to create a nuclear-spin-free environment in this material platform, thus mitigating existing

limitations for spin-based quantum information processing applications. For these reasons, Ge quantum wells constitute a promising platform for realizing semiconductor spin qubits and hybrid Andreev qubits [25]. Initial investigations of ABSs in Ge quantum wells have revealed the feasibility of this platform for realizing hybrid quantum devices [19,26]; however, the physical mechanisms affecting ABS energies in Ge-based JJs are not yet well understood.

Here, we used microwave spectroscopy techniques to study ABSs in JJs of various lengths realized in Ge quantum wells. These junctions were embedded in superconducting loops, which were inductively coupled to Nb coplanar waveguide resonators using the flip-chip approach [15,17,19,27]. This technique enabled us to reduce dielectric losses by separating the superconducting resonators from the Ge heterostructure with a vacuum gap, resulting in high resonator internal quality factors. Improved readout sensitivity compared to our previous work [19] enabled observation of previously unseen features in microwave spectroscopy measurements, namely single-quasiparticle transitions (SQPTs) and mixed pair transitions (PTs). The experimentally measured ABS spectra were reproduced by models incorporating multiple interacting ABSs in the junction, providing good qualitative agreement. For a junction of length L shorter than the superconducting coherence length of Ge ξ_{Ge} , ABS

*Contact author: fni@zurich.ibm.com

†Contact author: Deividas.Sabonis@ibm.com

Published by the American Physical Society under the terms of the [Creative Commons Attribution 4.0 International](https://creativecommons.org/licenses/by/4.0/) license. Further distribution of this work must maintain attribution to the author(s) and the published article's title, journal citation, and DOI.

spectra contained multiple PTs and an SQPT. Moreover, in a long junction with $L > \xi_{\text{Ge}}$, many PTs and SQPTs were observed. Coulomb interaction shifted the transition frequencies depending on the quasiparticle (QP) occupation of ABSs, lifting the degeneracy between two SQPTs. These results highlight the importance of finite-length effects and Coulomb interaction in JJs realized in Ge quantum wells.

II. DEVICES AND RESONATOR CHARACTERIZATION

Two devices, named device 1 and device 2, were realized in strained Ge quantum wells grown with reduced-pressure chemical vapor deposition [29]. Figure 1(a) shows a schematic of device 1, comprising a JJ embedded in a superconducting PtSiGe loop (purple), with two gate electrodes (yellow) and a flux line (blue), which was absent for device 2. The PtSiGe contacts were fabricated via Pt lift off and rapid thermal annealing [23]. An SiO_x dielectric layer was deposited with atomic-layer deposition, and the gates and flux line were then formed by lift off of Ti/Al/Ti/Au. Appendix A contains details of the fabrication procedure. The voltage V_g applied to the accumulation gate controlled the hole density in the Ge quantum well, which was insulating for $V_g = 0$. Unless specified otherwise, no dc voltage was applied to the side gate ($V_s = 0$). Instead, this gate was used for applying the rf drive tone for two-tone spectroscopy measurements via a bias tee. The phase difference across the junction φ was controlled with a magnetic flux Φ , which we applied by injecting a current I into the flux line (device 1) or into a superconducting coil in the vicinity of the sample (device 2). Due to the low kinetic inductance of the PtSiGe loops, we use the relation $\varphi = 2\pi\Phi/\Phi_0$, where Φ_0 is the superconducting flux quantum.

False-colored scanning electron micrographs of two exemplary junctions (top view) are shown in Figs. 1(b) and 1(c). Device 1 consisted of a lithographically defined junction with length $L = 350$ nm and width $W = 100$ nm, whereas for device 2, $L = 1.2$ μm and $W = 150$ nm. The superconducting coherence length in Ge was estimated using the Bardeen-Cooper-Schrieffer expression [30] $\xi_{\text{Ge}} = \hbar v_F / \pi \Delta_0 \approx 900$ nm, where $\Delta_0 \approx 60$ μeV (14.5 GHz) is the induced superconducting gap at $T = 0$ extracted from multiple-Andreev-reflection measurements and $v_F \approx 2.5 \times 10^5$ m s^{-1} is the Fermi velocity extracted from Hall-bar measurements [19] using an effective mass of $0.06m_e$ [24]. Since device 1 had a junction length smaller than the estimated coherence length, $L < \xi_{\text{Ge}}$, this device was expected to conform to the short-junction regime [19]. For device 2, $L > \xi_{\text{Ge}}$, placing this device in the long-junction regime. The finite width of the devices implies that they could host multiple transverse conduction channels.

Figure 1(d) depicts an optical microscope image of a sample after flip-chip bonding and subsequent wire bonding. A high-resistivity Si chip (resonator chip) contained a superconducting feedline with three capacitively coupled $\lambda/4$ Nb coplanar waveguide resonators. During flip-chip bonding, the grounded ends of the Nb resonators on the resonator chip were aligned to the superconducting loops of the Ge devices on the device chip, resulting in inductive coupling. The two chips were connected via In bumps for electrical connections and mechanical stability, enabling application of dc and rf signals to the devices through wire bonds on the resonator chip. More details of the measurement circuit can be found in Refs. [17,19].

For microwave measurements, a vector network analyzer (VNA) was used to apply a continuous readout tone with frequency f_r close to the resonance frequency of the resonator f_{res} . The readout tone was transmitted through the feedline where it interacted with the resonator, and after amplification at various temperature stages of the dilution refrigerator, the VNA detected the outgoing signal and determined the complex scattering parameter S_{21} . Figures 1(e) and 1(f) depict resonator traces, measured at $V_g = 0$, yielding the bare resonator frequencies $f_0 = 6.90115$ GHz for device 1 and $f_0 = 6.86731$ GHz for device 2. The internal (Q_i) and loaded (Q_L) quality factors of the resonators, obtained with the circle-fit method [28], were 70 000 and 23 000, respectively, for device 1 and 355 000 and 39 000, respectively, for device 2. The large difference between the quality factors was attributed to the presence of the flux line for device 1, which was aligned parallel to the resonator and thus likely contributed to the microwave losses [31].

Two-tone microwave spectroscopy was performed by applying a drive tone with power P_d and frequency f_d to the side gate, in addition to the readout tone. Whenever the drive-tone frequency was equal to a transition frequency $f_d = \Delta E/h$ between different levels in the ABS energy spectrum, the frequency of the resonator acquired a dispersive shift and damping, enabling the detection of ABS transition frequencies [8–11,13–20,32–34]. Resonator compensation, as described in Appendix C, was conducted at each value of the gate voltage V_g or phase φ , such that two-tone spectroscopy was performed at a readout frequency with a fixed offset from f_{res} , which changed as a function of V_g and φ .

III. MICROWAVE SPECTROSCOPY OF DEVICE 1

We first present microwave measurements on device 1, which had a length $L = 350$ nm, smaller than the superconducting coherence length of Ge. Figure 2(a) shows the amplitude R of the resonator transmission as a function of the offset readout frequency $f_r - f_0$ and the phase difference across the junction φ at a gate voltage $V_g = -0.7650$ V. The amplitude R is given by $R = \sqrt{I^2 + Q^2}$, where I

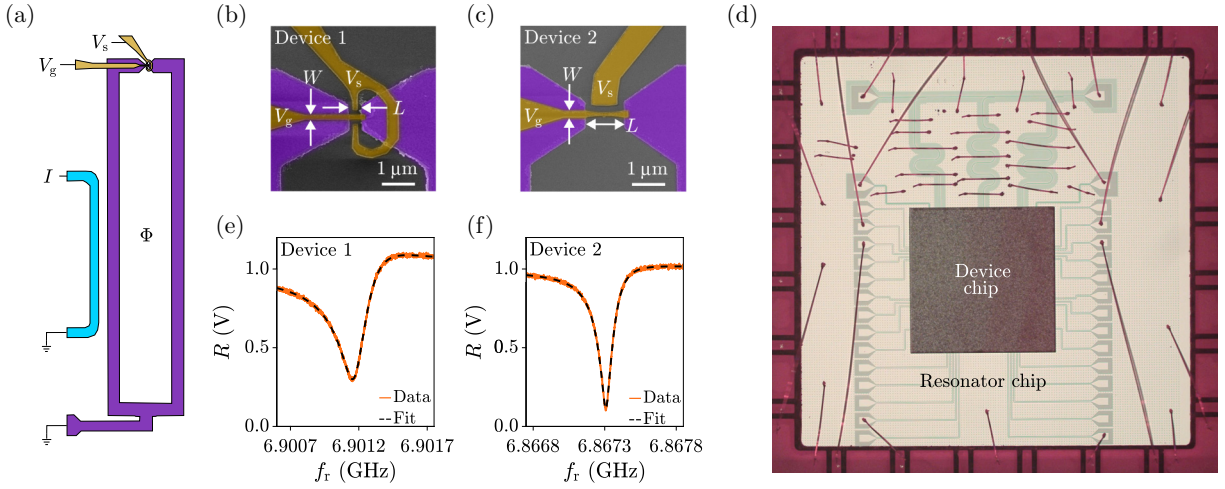


FIG. 1. (a) Schematic of device 1, consisting of a PtSiGe superconducting loop (purple), Ti/Al/Ti/Au gates (yellow), and a Ti/Al/Ti/Au flux line (blue). The dc voltage V_g controlled the hole density in the Ge quantum well via the accumulation gate. The rf drive tone for two-tone spectroscopy measurements was applied via the side gate indicated with V_s using a bias tee. For device 1, the magnetic flux Φ was controlled by passing a current I through the flux line, while for device 2, Φ was controlled via a superconducting coil mounted in the vicinity of the sample. (b),(c) False-colored scanning electron micrographs (top view) of exemplary Josephson junctions, identical to (b) device 1 and (c) device 2. The dimensions of each junction are defined by the separation L between the superconducting PtSiGe electrodes (purple) and the width W of the metallic accumulation gate (yellow). The side gate (yellow) was used to apply the rf drive tone. The gates were separated from the Ge heterostructure by an SiO_x dielectric layer (not visible). (d) Optical microscope image after flip-chip bonding and wire bonding. The device chip ($3 \times 3 \text{ mm}^2$) hosting the Ge quantum well was connected to the resonator chip ($10 \times 10 \text{ mm}^2$) via In bumps. The grounded ends of the $\lambda/4$ Nb resonators were aligned to the superconducting loops of the devices (not visible). (e),(f) Amplitude $R = \sqrt{I^2 + Q^2}$ of the resonator transmission S_{21} (normalized) as a function of readout frequency f_r for (e) device 1 and (f) device 2. The dashed black lines are fits to the data obtained using the circle-fit method [28].

and Q are the in-phase and quadrature components of the resonator response, respectively. The modulation of the resonance frequency of the resonator f_{res} with phase φ was fitted following Refs. [17,35], yielding a critical current of $I_C = 3.1 \text{ nA}$. Assuming that a single ABS can carry up to 7 nA of current [36], this is consistent with one or very few ABSs in the junction at this value of V_g .

A two-tone spectroscopy measurement is shown in Fig. 2(b), acquired together with the single-tone measurement in Fig. 2(a). Here, the amplitude R is shown as a function of the drive-tone frequency f_d and the phase difference across the junction φ . We observed a single transition, corresponding to a pair transition (PT) with frequency $f_1 = (2E_1)/h$, as schematically shown in Fig. 3(b). To account for the finite length of the junction, which results in detachment of the ABS from the continuum for a ballistic channel, the following dispersion relation [21] was used for the ABS energy:

$$E_i(\varphi) = \pm \tilde{\Delta}_i \sqrt{1 - \tau_i \sin^2(\varphi/2)}, \quad (1)$$

where $\tilde{\Delta}_i$ is the ABS amplitude and τ_i is the transmission of the state. Equation (1) is similar to the short-junction ABS dispersion relation [3,36], except that $\tilde{\Delta}_i < \Delta$, where Δ is the induced superconducting gap. Fitting the data in

Fig. 2(b) to Eq. (1) yielded $\tilde{\Delta}/h \approx 9.5 \text{ GHz}$ and $\tau \approx 0.80$. The fit is plotted as a black dashed line in the left half of Fig. 2(b).

The ABS spectrum changed drastically when the hole density in the junction was decreased, as shown in Figs. 2(c) and 2(d) at $V_g = -0.7443 \text{ V}$. The resonator trace in Fig. 2(c) displays anticrossings around $\varphi = \pm\pi$ (red arrows), indicating that the ABS transition frequency f_1 crossed the resonator frequency f_{res} at these values of the phase, resulting in ABS-resonator interaction [13]. Due to the anticrossings, it was not possible to fit the modulation in f_{res} with the procedure used for Fig. 2(a). The two-tone spectroscopy measurement in Fig. 2(d) showed a PT with minima in the transition frequency at $\varphi = \pm\pi$ and an SQPT, characterized by a minimum in the transition frequency at $\varphi = 0$. The latter corresponds to a QP being excited from one ABS to another, resulting in a transition frequency $f = (E_2 - E_1)/h$. Observation of this SQPT implies that the junction hosted more than one ABS at this value of V_g . The SQPT was reproduced with the finite-length model of Eq. (1) by considering two ABSs with $\tilde{\Delta}_1/h = 0.42\Delta/h \approx 6.1 \text{ GHz}$ ($\Delta = 14.5 \text{ GHz}$) and $\tau_1 = 0.78$ for the first ABS, and $\tilde{\Delta}_2/h = \Delta/h = 14.5 \text{ GHz}$ and $\tau_2 = 0.20$ for the second ABS. The high value of $\tilde{\Delta}_2$ and low value of τ_2 indicate that the energy of the

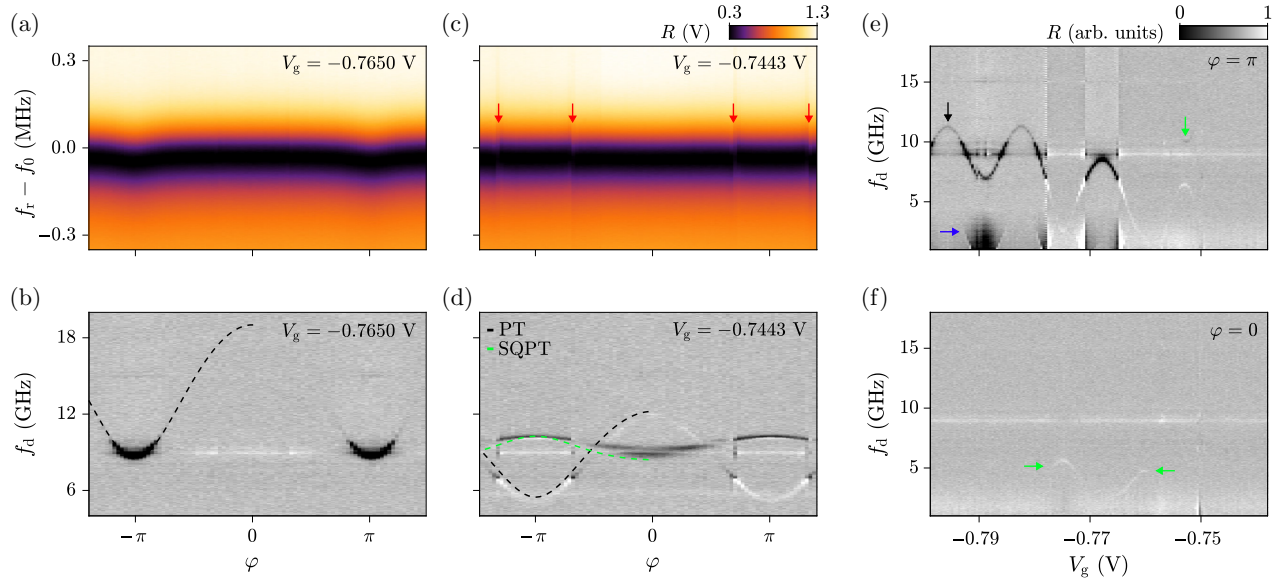


FIG. 2. (a) Device 1: amplitude R of the resonator transmission S_{21} as a function of offset readout frequency $f_r - f_0$ and phase φ at gate voltage $V_g = -0.7650$ V, with $f_0 = 6.90115$ GHz. (b) Amplitude R of the resonator transmission S_{21} as a function of drive frequency f_d ($P_d = -26$ dBm) and phase φ , measured together with (a). A single Andreev bound state (ABS) pair transition (PT) was observed. The black dashed line is a fit to the PT frequency $f_1 = (2E_1)/h$ using Eq. (1) for E_1 . (c) Same as (a), measured at $V_g = -0.7443$ V. Anticrossings (red arrows) indicate ABS interaction with the resonator. (d) Same as (b), measured together with (c). In addition to the PT, a single-quasiparticle transition (SQPT) was observed, indicating the presence of two ABSs. The black dashed line is a fit to the PT $f_1 = (2E_1)/h$, and the green dashed line corresponds to the SQPT with frequency $f = (E_2 - E_1)/h$, where E_1 and E_2 are given by Eq. (1). (e) Amplitude R of the resonator transmission S_{21} as a function of drive frequency f_d ($P_d = -25$ dBm) and gate voltage V_g , measured at $\varphi = \pi$. The PT (black arrow) was observed over nearly the full range of V_g . The dark-blue horizontal arrow indicates a replica of the PT. The SQPT is visible around $V_g = -0.7550$ V (green arrow). (f) Same as (e), measured at $\varphi = 0$. The SQPT appeared in a limited range of V_g , indicated with green arrows.

second ABS remained close to the superconducting gap Δ , with weak dispersion. The PT associated with the second ABS with frequency $f_2 = (2E_2)/h$ is outside the spectral range of Fig. 2(d). Therefore, the second ABS was only observed indirectly via the SQPT. Note that sign inversions of the shift in R occurred whenever the ABS transition frequency crossed the resonator frequency at $f_d = f_{\text{res}} \approx 6.90115$ GHz, resulting from a change in the direction of the resonator dispersive shift. Moreover, the dispersive shift is opposite for PTs and SQPTs [34].

The evolution of the ABS transition frequencies with the gate voltage V_g is depicted in Figs. 2(e) and 2(f) at phases $\varphi = \pi$ and $\varphi = 0$, respectively. These two-tone spectroscopy measurements were acquired together, where for each value of V_g , resonator compensation and a two-tone spectroscopy measurement were performed at both $\varphi = \pi$ and $\varphi = 0$ (Appendix D). The PT corresponding to the first ABS, indicated with a black arrow in Fig. 2(e), was observed over nearly the full range of V_g at $\varphi = \pi$, with replicas appearing at 6.9 GHz below the transition frequency, indicated with a dark-blue horizontal arrow. Such replicas are commonly observed in two-tone spectroscopy measurements and are attributed to multiphoton processes involving resonator photons with energy $E = hf_{\text{res}}$ [15,17].

In addition, the SQPT was observed around $V_g = -0.7550$ V [green arrow in Fig. 2(e)]. For the measurement performed at $\varphi = 0$ in Fig. 2(f), the PT with $f_1(\varphi = 0) > f_1(\varphi = \pi)$ was not observed. Instead, the SQPT is visible in a finite range of V_g , indicated with green arrows. The appearance of the SQPT for a limited range of V_g values might be due to opening and closing of the second conduction channel and oscillations of the second ABS, similar to those of the first ABS in Fig. 2(e). Mesoscopic fluctuations of the ABS energy as a function of gate voltage have also been reported for JJs realized in nanowires and two-dimensional electron gases [10,15,17,18,20,37]. Due to gate-voltage-induced hysteresis, which was measured in the same material [38], the transition frequencies at $\varphi = 0$ and $\varphi = \pi$ in Figs. 2(a)–2(d) deviate from those in Figs. 2(e) and 2(f) at the corresponding values of V_g . The gate dependence of an additional device, with similar dimensions to device 1, is presented in Appendix E.

In summary, device 1 showed finite-length effects despite the junction length being shorter than the estimated superconducting coherence length of Ge. Moreover, readout improvements enabled the observation of an SQPT, previously not detected for similar junctions [19].

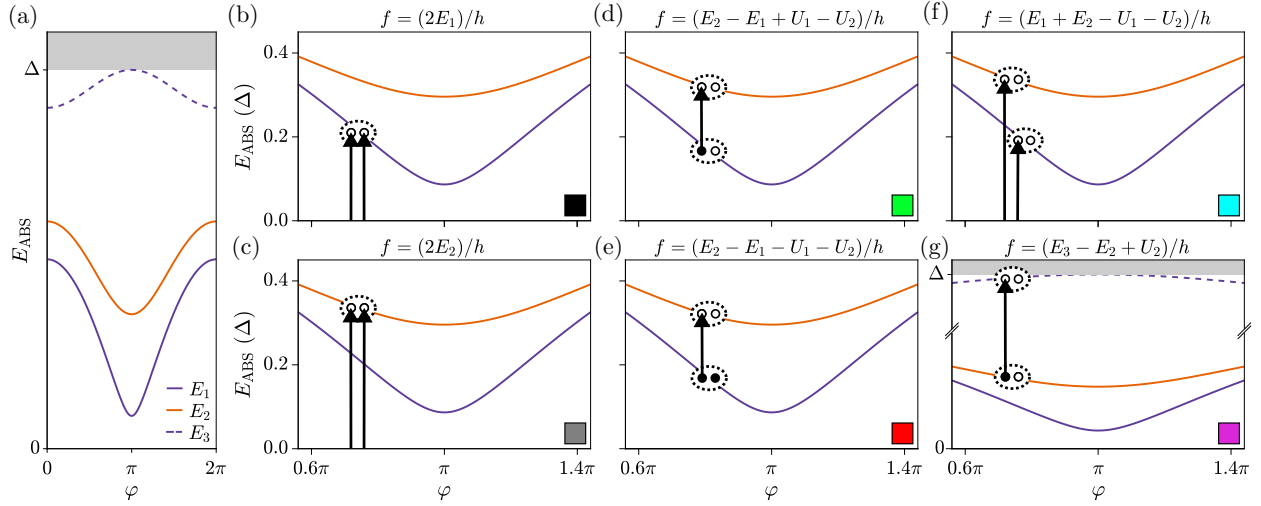


FIG. 3. (a) Energy spectrum of a long junction hosting three spin-degenerate ABSs in two conduction channels (purple, orange) with energies E_1 (purple, solid line), E_2 (orange, solid line), and E_3 (purple, dashed line) as a function of the phase difference across the junction φ , shown in the excitation picture. The continuum above the induced superconducting gap Δ is indicated with gray shading. Coulomb interaction manifests as an energy penalty U_i given by Eq. (2) for states with even occupation. (b) Enlarged view of the energy spectrum in (a). The PT for the ABS with energy E_1 is indicated with arrows. The transition frequency is $f = (2E_1)/h$. (c) PT for the ABS with energy E_2 , resulting in the transition frequency $f = (2E_2)/h$. (d) SQPT from E_1 to E_2 . The energy levels are shifted as a result of Coulomb interaction, yielding the transition frequency $f = (E_2 - E_1 + U_1 - U_2)/h$. (e) Same as (d), but with the first ABS initially in an excited state, resulting in $f = (E_2 - E_1 - U_1 - U_2)/h$. (f) Mixed PT with frequency $f = (E_1 + E_2 - U_1 - U_2)/h$. (g) SQPT from E_2 to E_3 . Since Coulomb interaction is neglected for E_3 due to its close proximity to the continuum, the SQPT frequency is given by $f = (E_3 - E_2 + U_2)/h$.

These transitions are particularly interesting for studies of spin-orbit interaction in long junctions [10–12,14,18].

IV. COULOMB INTERACTION IN A LONG JUNCTION

For junctions with length $L \sim \xi$, QPs have a finite dwell time in the junction region, and interactions therefore affect the ABS physics. In particular, Coulomb interaction leads to energy shifts in the ABS spectrum [14,16,21,22]. To reproduce the experimentally observed ABS transitions presented in the next section, we consider a long junction with two conduction channels, each of which can host up to two ABSs. The corresponding ABS transitions, as well as the effects of Coulomb interaction, are discussed here.

Figure 3(a) schematically depicts the energy spectrum of a finite-length junction with two conduction channels hosting three spin-degenerate ABSs, E_1 (solid line) and E_3 (dashed line) in one conduction channel (purple) and E_2 (solid line) in the second conduction channel (orange). The energy of the first ABS, E_1 , is smaller than the energy of the second ABS, E_2 . Since the energy spectrum is symmetric around zero energy, the excitation picture is used here, for which only the positive part of the energy spectrum is depicted. The ABS energies E_i are approximated by Eq. (1). We note that away from $\varphi = \pi$ and $\varphi = 0$, a more accurate description of the ABS energies is given

by the solutions to the Bogoliubov-de Gennes Hamiltonian [10,14,18,39]. As a result of Coulomb interaction in the junction, the energies of the many-body states shift depending on the population of the ABSs. Since the charge of a QP depends on its energy, the phase dependence of the Coulomb interaction energy U_i for an ABS with energy E_i from Eq. (1) is estimated as [22]

$$U_i(\varphi) = \begin{cases} u_i [\Delta^2 - E_i(\varphi)^2], & n = 0, 2, \\ 0, & n = 1, \end{cases} \quad (2)$$

where n is the number of QPs occupying an ABS and u_i is a constant, defined by the microscopic details of the corresponding state and the extension of the wave function into the superconducting leads; see Appendix F. Each ABS can host up to two QPs. For states occupied by a single QP, particle-hole symmetry implies that $U_i(\varphi) = 0$. Instead, states with even occupation, i.e., zero or two QPs, are shifted to higher energy by $+U_i(\varphi)$ [16,21]. Consequently, the frequencies of certain ABS transitions are affected by Coulomb interaction. In Figs. 3(b)–3(g), different transitions involving the two lowest-energy ABSs E_1 and E_2 [Figs. 3(b)–3(f)] and the third ABS E_3 [Fig. 3(g)] are schematically illustrated. Below, we discuss the effects of Coulomb interaction on these transitions. We neglect Coulomb interaction for E_3 since the energy of this state is

close to the continuum edge Δ . More details are reported in Appendix F.

During a PT, two QPs are excited from the ground state to the ABS. Figure 3(b) shows the PT for the first ABS with energy E_1 (purple), where E_1 is given by Eq. (1). Before and after the PT, the energy of the ABS is shifted by $+U_1$ since the occupation of the state is even. Therefore, the energy change due to the PT, which determines the transition frequency, is given by $\Delta E = 2(E_1 + U_1) - 2U_1 = 2E_1$, yielding $f = (2E_1)/h$ for the PT. Accordingly, the frequencies of all PTs are not affected by Coulomb interaction. The PT for the second ABS with energy E_2 (orange) is shown in Fig. 3(c) with transition frequency $f = (2E_2)/h$.

Coulomb interaction modifies the frequency of the SQPT from E_1 to E_2 in Fig. 3(d). Before the SQPT, the energy is given by $E_1 + U_2$, because a single QP occupies E_1 , resulting in no energy shift for this level, and the unoccupied level E_2 is shifted by $+U_2$. After the QP is excited to E_2 , the energy is given by $E_2 + U_1$, as the first ABS is now unoccupied, giving rise to an energy shift of $+U_1$, while the second ABS hosting one QP has no energy shift. Consequently, the frequency of the SQPT in Fig. 3(d) is given by $f = (E_2 - E_1 + U_1 - U_2)/h$, whereas $f = (E_2 - E_1)/h$ in the absence of Coulomb interaction. If E_1 is initially in an excited state with full occupation, as shown in Fig. 3(e), before the SQPT, both E_1 and E_2 have even occupation, and after the SQPT both states are occupied by a single QP, resulting in an SQPT frequency $f = [E_2 - (E_1 + U_1 + U_2)]/h$ instead of $f = (E_2 - E_1)/h$ without Coulomb interaction. Hence, an important consequence of Coulomb interaction is that the degeneracy between the frequencies of the SQPTs in Figs. 3(d) and 3(e) is lifted. The frequency of the mixed PT in Fig. 3(f) is also modified by Coulomb interaction. Here, $f = (E_1 + E_2 - U_1 - U_2)/h$ since the energy before the transition is $U_1 + U_2$, while the energy after the transition is $E_1 + E_2$. Without Coulomb interaction, $f = (E_1 + E_2)/h$ for the mixed PT. Finally, the SQPT to the third ABS shown in Fig. 3(g) has a transition frequency given by $f = (E_3 - E_2 + U_2)/h$, since we neglect Coulomb interaction for E_3 . Experimentally, the signatures of Coulomb interaction are shifts of the SQPT and PT frequencies with respect to those associated with the ABS energies E_i .

V. MICROWAVE SPECTROSCOPY OF DEVICE 2

Device 2 had a junction length $L = 1.2 \mu\text{m}$, larger than the superconducting coherence length of Ge. Two-tone spectroscopy measurements in Fig. 4 revealed the presence of multiple ABSs in the junction. Figure 4(a) depicts the amplitude R of the resonator transmission S_{21} as a function of the phase difference across the junction φ and the drive-tone frequency f_d , at $V_g = -0.7990$ V. Multiple transitions are visible in the ABS spectrum, with varying linewidth and intensity. Similar to device 1, sign inversions of the

shift in R occur whenever a transition frequency crosses the resonator frequency f_{res} , and the shift is opposite for PTs with minima at $\varphi = \pi$ and SQPTs with maxima at $\varphi = \pi$. The presence of multiple SQPTs implied that the junction hosted several ABSs for this gate configuration. The observations were explained by a model considering three ABSs in the junction with Coulomb interaction, introduced in the previous section. The ABS energies E_1 and E_2 are given by Eq. (1) with $\tilde{\Delta}_1/h = 0.48\Delta/h \approx 7.0$ GHz and $\tau_1 = 0.98$, and $\tilde{\Delta}_2/h = 0.54\Delta/h \approx 7.8$ GHz and $\tau_2 = 0.72$, while E_3 was approximated using a cosine function, since this ABS was close to the continuum edge with weak dispersion and was therefore only observed indirectly (see Appendix F). The PTs to E_1 and E_2 are depicted as black and gray dashed lines in Fig. 4(b), matching the color of the square symbols in Figs. 3(b) and 3(c). Moreover, a replica of E_2 was observed, shifted downward by the resonator frequency to $f_d = f_2 - 6.9$ GHz. This replica is indicated with a gray dotted line in Fig. 4(b). The SQPTs between E_1 and E_2 , indicated with green and red dashed lines, respectively, correspond to the transitions in Figs. 3(d) and 3(e), while the SQPT from E_2 to E_3 , marked with a purple dashed line, corresponds to Fig. 3(g). The mixed PT, schematically shown in Fig. 3(f), is indicated with a cyan dashed line in Fig. 4(b). Moreover, the transition at slightly higher energy than the mixed PT can likely be identified as a two-photon transition (2-PhT) [8] involving the PT to E_1 and a resonator photon with energy hf_{res} , which yields the transition frequency $f = (2E_1 + hf_{\text{res}})/2h$, indicated with an orange dashed line in Fig. 4(b). Presumably, this 2-PhT was observed because the frequency of this PT crossed the resonator frequency, as evidenced by the single-tone spectroscopy measurements in Appendix G.

Changing the gate voltage modified the ABS spectrum significantly. In Fig. 4(c), we show another two-tone spectroscopy measurement of device 2, at a gate voltage $V_g = -0.6994$ V, with the side-gate voltage at $V_s = -0.0090$ V. Here, in addition to two PTs with minima at $\varphi = \pm\pi$, two SQPTs with distinct maxima at $\varphi = \pm\pi$ were observed, indicating the presence of a third ABS for this gate voltage configuration as well. The ABS energies E_1 and E_2 were found with Eq. (1) using $\tilde{\Delta}_1/h = 0.50\Delta \approx 7.3$ GHz and $\tau_1 = 0.62$, and $\tilde{\Delta}_2/h = 0.52\Delta \approx 7.5$ GHz and $\tau_2 = 0.51$. Again, the ABS with energy E_3 resided close to the continuum edge and thus it was approximated using a cosine function (Appendix F). Consequently, the PT to E_3 was outside the spectral range of the measurement. The PTs to E_1 and E_2 are indicated with black and gray dashed lines in Fig. 4(d). The minima of the PTs were slightly different at $\varphi = -\pi$ and $\varphi = \pi$, which we attributed to gate-voltage instabilities in the device; see also Appendix H. Due to the small energy difference between E_1 and E_2 , SQPTs between these states, shown in Figs. 3(d) and 3(e), were not observed here. Instead, the SQPTs from E_1 to E_3 (yellow dashed line) and E_2 to E_3 (purple dashed line) matched

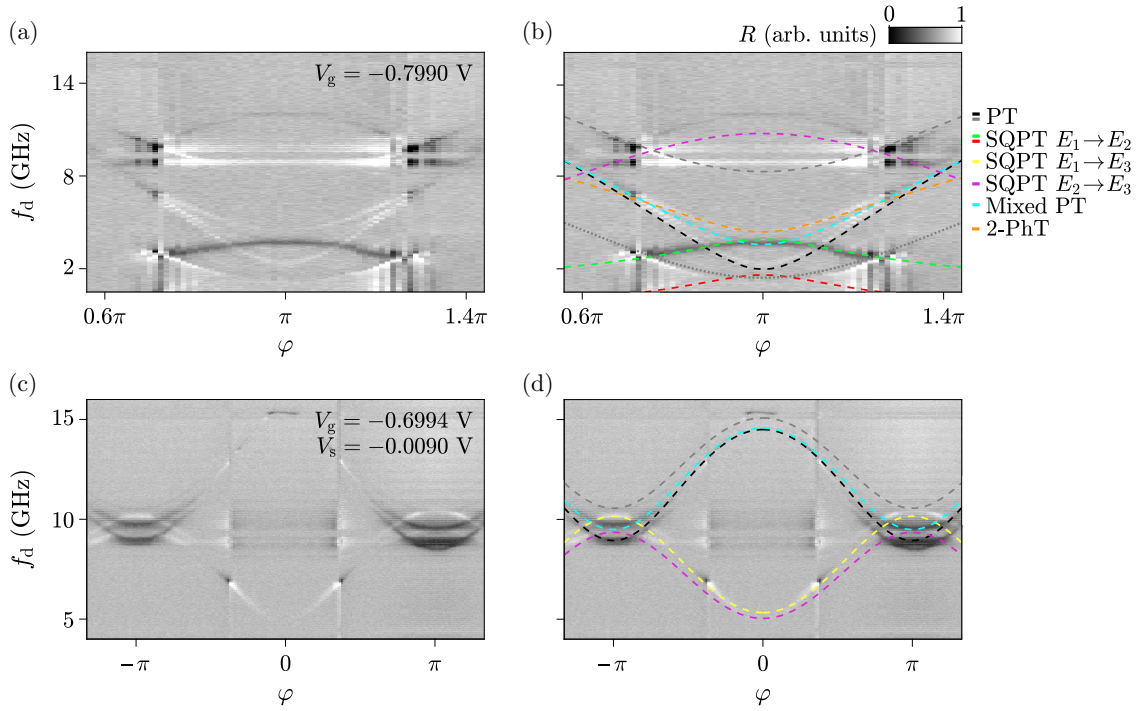


FIG. 4. (a) Device 2: amplitude R of the resonator transmission S_{21} as a function of drive frequency f_d ($P_d = -28$ dBm) and phase φ , measured at $V_g = -0.7990$ V. Multiple PTs and SQPTs are visible around $\varphi = \pi$. (b) Same as (a) but overlaid with ABS transitions predicted by the long-junction model with three ABSs and including Coulomb interaction. The black and gray dashed lines are PTs, schematically shown in Figs. 3(b) and 3(c). The gray dotted line is a replica of the gray PT, shifted downward by the resonator frequency $f_{\text{res}} \approx 6.86731$ GHz. The green, red, and purple dashed lines are SQPTs corresponding to Figs. 3(d), 3(e), and 3(g), respectively. The cyan line is a mixed PT [Fig. 3(f)] and the orange line is a two-photon transition (2-PhT) involving the lowest-energy PT and a resonator photon with energy $E = \hbar f_{\text{res}}$. (c) Same as (a) but measured over a wider range of φ and at $V_g = -0.6994$ V and $V_s = -0.0090$ V ($P_d = -35$ dBm). At this gate-voltage configuration, several PTs and SQPTs were observed. (d) Same as (c), overlaid with ABS transitions predicted by the model. The transitions are colored according to the legend in (b). Here, the yellow dashed line is an SQPT from the lowest-energy ABS E_1 to the highest-energy ABS E_3 .

the experimental data. The frequency difference between these SQPTs was enhanced by the Coulomb interaction, which was stronger for the first ABS. This is evident from Eq. (2), where the Coulomb interaction energy U_i is larger for lower E_i . The other transition in Fig. 4(c) with minima at $\varphi = \pm\pi$ corresponds to the mixed PT between E_1 and E_2 and is indicated with a cyan dashed line in Fig. 4(d). Finally, we note that fewer transitions are visible in Fig. 4(c) than in Fig. 4(a), which could be related to the different gate voltages or the lower drive power P_d used for Fig. 4(d).

The experimental data are in good agreement with the model, apart from the SQPT from E_1 to E_3 in Fig. 4(b) (purple dashed line), for which the model predicts slightly lower transition frequencies. To achieve better quantitative agreement between the measured and predicted transition frequencies, higher-order terms in the Coulomb interaction, as well as the exchange interaction [14,18], would need to be included in the model.

We note that signatures of spin splitting in ABSs, reported for long junctions in InAs nanowires [10–12,14,

15,18], were not observed in our devices. This is surprising, as device 2 conformed to the long-junction regime and showed several SQPT and mixed-PT transitions, which generally evidence spin-orbit effects. We therefore conclude that spin-orbit interaction in our devices is weak, which is presumably related to strain in the Ge quantum well [40,41] or the junction geometry [42], both of which suppress spin-orbit interaction. Furthermore, two-dimensional hole gases have a cubic Rashba spin-orbit interaction, where spin splitting for low carrier density is expected to be small [43]. Spin-orbit interaction can likely be strengthened by engineering the material stack. Strain in the quantum well might be reduced by optimizing the stoichiometry of the SiGe barriers and buffer layers. In addition, it was recently shown that spin-orbit interaction was enhanced in an unstrained Ge-SiGe heterojunction [44].

Several transitions are predicted by the model with frequencies outside the spectral range of the measurements. Not only was the setup limited by the frequency range of the VNA (26 GHz), but the intensity of transitions also

decreased as the detuning from the resonator increased. To measure transitions at high frequencies, the coupling between the resonator and the ABS would need to be improved. This is a limitation of the flip-chip approach, where the air gap between the resonator and device chips limits the strength of the inductive coupling to several MHz [19]. Nonetheless, future work could focus on optimizing the resonator-ABS coupling strength by decreasing the air gap between the flip-chip-bonded chips, modifying the resonator frequency or investigating different types of resonators [45].

VI. CONCLUSION

In summary, we performed microwave spectroscopy measurements of Andreev bound states in Josephson junctions shorter and longer than the superconducting coherence length, realized in proximitized Ge quantum wells. Flip-chip bonding enabled inductive coupling between superconducting PtSiGe loops and Nb coplanar waveguide resonators, resulting in high quality factors. Two-tone microwave spectroscopy measurements of a 350-nm-long junction revealed a single-quasiparticle transition in a limited range of gate-voltage values, previously not observed in similar devices [19]. We developed a model that was able to reproduce the experimental data by taking the finite length of the junction into account. Our model revealed the presence of a second ABS whose energy was outside the spectral range of the measurements. A device consisting of a junction with length 1.2 μm was also investigated. Several ABS transitions were measured with two-tone spectroscopy, indicative of multiple interacting ABSs in the junction. The experimentally observed transitions were reproduced with a model comprising three ABSs in two conducting channels with finite Coulomb interaction, which provided good qualitative fits to the observations for multiple gate configurations.

We demonstrated the importance of including finite-length effects and Coulomb interaction in models describing ABSs in intermediate and long junctions. Next steps for understanding the ABS physics in proximitized Ge quantum wells include theoretical investigation of spin-orbit interaction in Ge-based Josephson junctions and experimental studies of dynamic processes, such as quasiparticle poisoning and parity switching, in devices where Coulomb interaction is prominent.

ACKNOWLEDGMENTS

We thank the Cleanroom Operations Team of the Binnig and Rohrer Nanotechnology Center (BRNC) for their help and support. We thank S. Bosco, B. van Heck, V. Coppini, J. Klinovaja, V. Kozin, M. Pita-Vidal, D. Z. Haxell, and H. Riel for useful discussions. J.C.C. thanks the Spanish Ministry of Science and Innovation (Grant No. PID2020-114880GB-I00) for financial support and the Deutsche

Forschungsgemeinschaft (DFG; German Research Foundation) via SFB 1432 for sponsoring his stay at the University of Konstanz as a Mercator Fellow. D.C.O., A.E.S., and W.B. acknowledge support from the Deutsche Forschungsgemeinschaft (DFG; German Research Foundation) via SFB 1432 (Project No. 425217212) and from the Excellence Strategy of the University of Konstanz via a Blue Sky project. F.N. acknowledges support from the Swiss National Science Foundation (Grant No. 200021 201082).

DATA AVAILABILITY

The data that support the findings of this article are openly available [46].

APPENDIX A: DEVICE FABRICATION

The Josephson junction devices studied here were realized using a SiGe heterostructure grown with reduced-pressure chemical vapor deposition [29]. The material stack consisted of a Ge layer directly grown on a Si wafer, followed by a SiGe layer with an increasing Si content, up to $\text{Si}_{0.2}\text{Ge}_{0.8}$. This stoichiometry was used for the buffer layers surrounding the 20-nm-thick Ge quantum well, located 48 nm below the surface. More details on the SiGe heterostructure can be found in Refs. [29,38]. The superconducting loops were realized by electron-beam lithography, evaporation, and lift off of Pt, followed by rapid thermal annealing at 350 $^{\circ}\text{C}$, resulting in superconducting germanosilicide (PtSiGe), directly contacting the Ge quantum well [19]. Prior to the Pt evaporation, the native oxide was removed by a short submersion in hydrofluoric acid (HF). To isolate the gates from the heterostructure, a 12-nm-thick layer of SiO_x was deposited using atomic-layer deposition. Then, the inner gates, close to the active areas of the devices, were fabricated by evaporation and lift off of Ti/Al/Ti/Au (5 nm/70 nm/5 nm/40 nm). After this, the outer gates and flux line, consisting of Ti/Al/Ti/Au (5 nm/300 nm/5 nm/50 nm), were evaporated. For device 2, a single gate layer was used to define the gates, made of Ti/Al/Ti/Au (5 nm/70 nm/5 nm/40 nm). Finally, the chip was diced into a $3 \times 3\text{-mm}^2$ piece for flip-chip bonding to a resonator chip.

The resonators were fabricated on a high-resistivity ($\rho > 10\text{ k}\Omega\text{cm}$) intrinsic Si wafer. After removal of the native oxide using HF, a 200-nm-thick layer of Nb was sputtered onto the surface of the wafer. Using an Al_2O_3 hard mask and inductively coupled plasma reactive-ion etching with Cl_2/Ar , the resonators, feedline and dc control lines, as well as ground-plane holes, were patterned into the Nb layer. For flip-chip bonding, In bumps were realized with evaporation and lift off. Prior to the In evaporation, the native oxide was removed using HF.

APPENDIX B: PACKAGING AND MEASUREMENT SETUP

The device and resonator chips were flip-chip bonded with a Karl Suss FC 150 flip-chip bonder. Alignment markers on both chips facilitated correct positioning of the device chip with respect to the resonator chip, with the superconducting device loops aligned to the grounded ends of the $\lambda/4$ coplanar waveguide resonators. After this, the resonator chip was clamped in the QDevil QCage.24 sample holder with an integrated superconducting coil for magnetic-flux biasing. Microwave and dc lines on the sample holder were connected to corresponding bonding pads on the resonator chip via wire bonding with Al bond wires. Moreover, Al air bridges across the resonators and feedline connected different areas of the ground plane, to establish a uniform ground potential across the resonator chip.

Measurements were performed in a Bluefors BF LD 400 cryogen-free dilution refrigerator with a mixing-chamber base temperature of 30 mK. Figure 5 schematically illustrates the wiring of the dilution refrigerator. A Keysight PNA-X VNA was used to apply a readout tone with power P_{in} and frequency f_r . Two-tone spectroscopy measurements were performed by applying a continuous drive tone of power P_d and frequency f_d with the same VNA. The readout and drive signals were attenuated by 66 and 26 dB, respectively. After propagating through the feedline, a circulator, and a dual isolator, the readout signal was amplified by a traveling-wave parametric amplifier (TWPA) with 20-dB gain at the mixing-chamber temperature stage of the dilution refrigerator. The TWPA was pumped by a continuous pump tone supplied by an R&S SGS100A signal generator and attenuated by 26 dB in

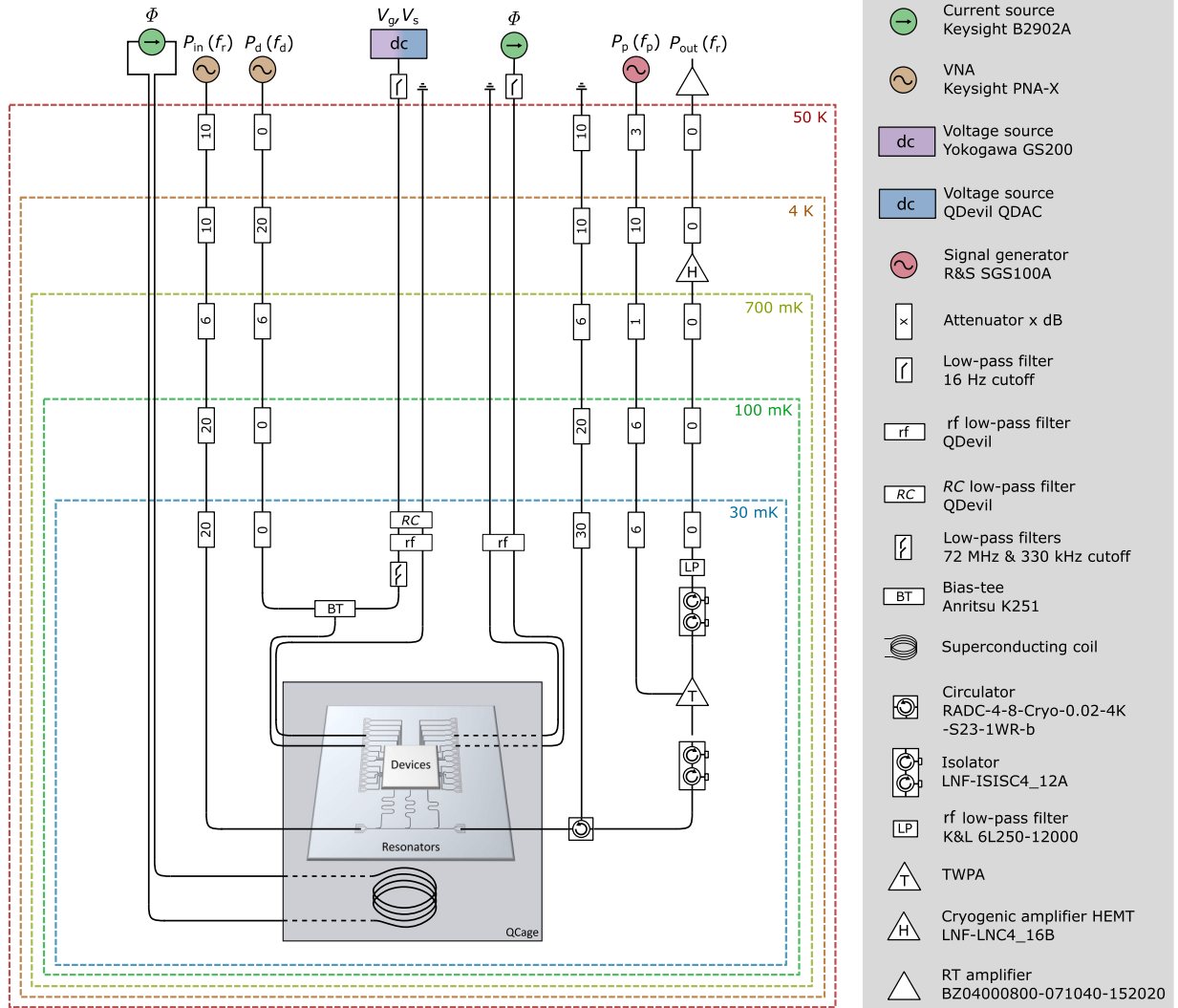


FIG. 5. Schematic representation of the flip-chip-bonded device in the QCage.24 sample holder, the dilution refrigerator used to perform the measurements, and the electronic setup.

the dilution refrigerator. Then, the readout signal passed through another dual isolator and a low-pass filter, before amplification by a cryogenic high-electron-mobility transistor (HEMT) amplifier with 36-dB gain, installed at the 4-K stage, and a room-temperature amplifier with 44-dB gain. The amplified signal was detected by the VNA, at the port labeled P_{out} in Fig. 5. The gate voltages V_g and V_s were applied by a Yokogawa GS200 dc voltage source (device 1) and a QDevil digital-to-analog converter dc voltage source (device 2). The dc signals were filtered by a home-made low-pass filter at room temperature and QDevil RC and rf filters at the mixing-chamber stage of the dilution refrigerator before passing through bias tees to combine dc and rf drive signals. For device 1, the magnetic flux threading the superconducting device loop was supplied by an on-chip flux line, which was current biased using a Keysight B2902A SMU. The current passed through a NbTi superconducting line, filtered by a QDevil rf filter at the mixing-chamber stage of the dilution refrigerator. For device 2, the magnetic flux was controlled by applying a current with the Keysight B2902A SMU to a superconducting coil integrated in the QCage.24 sample holder. The sample space was additionally shielded from external magnetic fields by a home-made magnetic shield comprising a μ -metal and superconducting sheet.

APPENDIX C: RESONATOR COMPENSATION

The two-tone spectroscopy measurements shown in Figs. 2 and 4 were acquired using resonator compensation. Each time, the slow-axis variable—i.e., gate voltage or magnetic flux (phase)—was changed, the drive tone was switched off and a resonator trace was measured, for which the readout frequency f_r was swept around the resonance frequency of the resonator, and the complex scattering parameter S_{21} was recorded to precisely determine f_{res} , the frequency of the minimum in the magnitude $|S_{21}|$. Then, the readout frequency f_r was fixed at $f_r = f_{\text{res}} + 50$ kHz, on the slope of the resonator trace, where the sensitivity of $|S_{21}|$ to shifts in f_{res} was high. After fixing the readout frequency, the drive tone with power P_d was applied to the device and a two-tone spectroscopy measurement was performed by recording S_{21} at the aforementioned fixed readout frequency f_r while sweeping the drive frequency f_d . For these measurements, the readout power was fixed at $P_{\text{in}} = -40$ dBm for device 1 (Fig. 2) and $P_{\text{in}} = -42$ dBm for device 2 (Fig. 4). Two-tone spectroscopy measurements were acquired with an integration time per point of 100 μ s and 500 averages.

During postprocessing of the two-tone spectroscopy data, the background was removed by subtracting the median along the drive-frequency axis for each value of the gate voltage or phase.

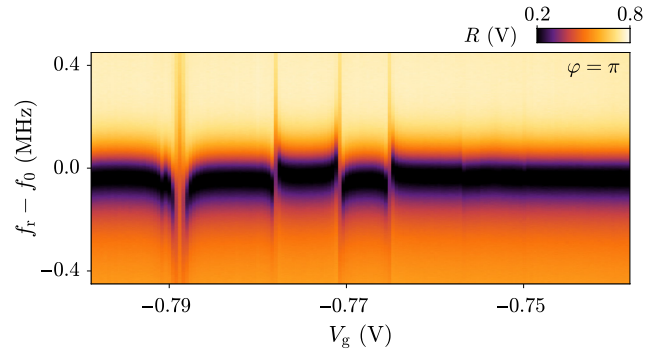


FIG. 6. Device 1: amplitude R of the resonator transmission S_{21} as a function of offset readout frequency $f_r - f_0$ and gate voltage V_g , with $f_0 = 6.90115$ GHz. The measurement was performed at $\varphi = \pi$ together with the two-tone spectroscopy measurement in Fig. 2(e).

APPENDIX D: DEVICE 1 GATE DEPENDENCE

The two-tone spectroscopy measurements as a function of gate voltage at $\varphi = \pi$ in Fig. 2(e) and $\varphi = 0$ in Fig. 2(f) were acquired together with resonator traces at each value of the gate voltage V_g to perform resonator compensation. In Fig. 6, the resonator traces at $\varphi = \pi$ are combined, yielding the amplitude R of the resonator transmission S_{21} as a function of the offset readout frequency $f_r - f_0$ and the gate voltage V_g . Anticrossings indicate interaction between the ABS and the resonator when the ABS transition frequency f_1 was equal to the resonance frequency of the resonator f_{res} . When f_1 was smaller than f_{res} , which is evident from the two-tone spectroscopy measurement in Fig. 2(e), the resonance frequency of the resonator f_{res} was shifted to higher frequencies than when $f_1 > f_{\text{res}}$.

APPENDIX E: DEVICE 3 GATE DEPENDENCE

We also investigated a third device, with a junction length identical to device 1, $L = 350$ nm, but with a slightly larger width, $W = 150$ nm. This device had a bare resonance frequency $f_0 = 5.83800$ GHz. The internal and loaded quality factors were $Q_i = 189\,000$ and $Q_L = 36\,000$, respectively, at $V_g = 0$. The gate dependence of this device is depicted in Fig. 7. Multiple anticrossings in Fig. 7(a) indicate that the ABS transition frequency crossed the resonator several times, similar to the gate dependence of device 1 in Fig. 6. The two-tone spectroscopy measurement in Fig. 7(b) revealed an oscillating ABS, which crossed the resonator at gate voltages corresponding to anticrossings in Fig. 7(a). The microwave line through which the drive tone was applied had 20 dB more attenuation than the microwave line used to apply the drive tone for devices 1 and 2. Therefore, a higher drive power P_d was used for the measurement in Fig. 7(b) than for the two-tone spectroscopy measurements in the main text. Moreover, for

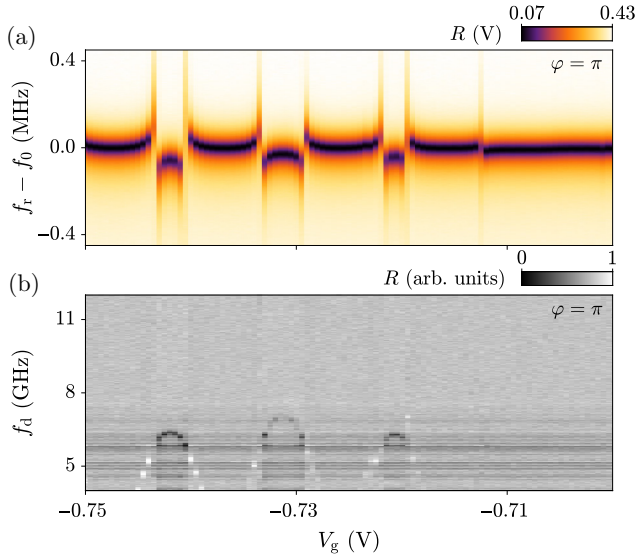


FIG. 7. (a) Device 3: amplitude R of the resonator transmission S_{21} as a function of offset readout frequency $f_r - f_0$ and gate voltage V_g , measured at $\varphi = \pi$, with $f_0 = 5.83800$ GHz. (b) Amplitude R as a function of drive frequency f_d ($P_d = -16$ dBm) and gate voltage V_g , measured together with (a).

this device, more standing waves were observed in the two-tone spectroscopy measurement. Nonetheless, the behavior of device 3 is similar to that of device 1.

APPENDIX F: THEORETICAL MODEL FOR FINITE JUNCTIONS

To theoretically describe a finite-length JJ, we consider a few conducting channels, each of which can potentially host multiple ABSs. For the length scales relevant to our experiment, each channel can accommodate up to two ABSs. Furthermore, we observe transitions corresponding to ABSs in two channels. This type of system has been studied in detail for InAs nanowires [10,14,21,39]. In our Ge-based system, no spin splitting of the ABSs is observed, likely due to the weak spin-orbit interaction, consistent with strain-induced suppression of spin-orbit coupling in Ge samples with strong confinement in a single direction [40].

For the long junction, we take into account the effect of interactions, as QPs have a finite dwell time in the junction region. As predicted theoretically [21] and observed experimentally [14,16], Coulomb interaction in intermediate-length junctions leads to finite shifts in the ABS spectrum. This interaction can be treated perturbatively due to the strong screening provided by the superconducting leads. The resulting effect is twofold. First, the wave function of a QP in the ABS of a ballistic junction extends into the superconducting leads, where the Coulomb interaction is screened. This reduces the effective interaction strength by a factor of Δ^2/Γ^2 , where Γ is the coupling to the leads;

TABLE I. Parameters used for obtaining ABS transition frequencies.

Figure	τ_1	τ_2	$\tilde{\Delta}_1/h$	$\tilde{\Delta}_2/h$	$\tilde{\Delta}_3/h$	u_1	u_2
4(b)	0.98	0.72	0.48Δ	0.54Δ	0.10Δ	0.08	0.03
4(d)	0.62	0.51	0.50Δ	0.52Δ	0.07Δ	0.01	0.01

for a ballistic channel, typically $\Gamma \gg \Delta$. Second, the QP charge is reduced, as it is a coherent superposition of an electron and a hole. This results in an energy-dependent effective charge. Consequently, the Coulomb energy is rescaled by approximately $[\Delta^2 - E_i^2(\varphi)]/\Delta^2$. Altogether, the Coulomb interaction for each ABS can be written as

$$U_i(\varphi) = U_{c,i} \frac{\Delta^2 - E_i^2(\varphi)}{\Gamma_i^2}, \quad (\text{F1})$$

where $U_{c,i} = e^2/C_i$ is the charging energy of an effective model quantum dot determined by microscopic details of the corresponding channel and C_i represents its self-capacitance [21]. Thus, the coefficients u_i in the main text are given by $u_i = (e^2/C_i)(1/\Gamma_i^2)$. Following Refs. [16,21,22], we see that the lowest-order correction due to Coulomb interaction adds $U_i(\varphi)$ for every evenly occupied ABS.

The phase dispersion of ABSs in a junction of intermediate length is more complex than for the short-junction regime [10,39]; however, the dispersion of the lowest-energy ABS in each channel (E_1 and E_2 in the main text) can be approximated by Eq. (1). The higher-energy ABS in the experiment (E_3) resides in close proximity to the continuum, with weak phase dispersion. Therefore, it can be approximated using a weak cosine dispersion with maxima at $\pi(2n+1)$, resulting in

$$E_3(\varphi) = \Delta - \tilde{\Delta}_3[1 + \cos(\varphi)]. \quad (\text{F2})$$

The curvature sign of the phase dispersion indicates that this state is the second ABS in the channel. Due to its close proximity to the continuum, the effective charge of a QP in this ABS is very small. Hence, Coulomb interaction in this ABS can be neglected.

Two different gate-voltage regimes are presented in Fig. 4 of the main text. The ABS transition frequencies are obtained with the parameters listed in Table I, where the induced superconducting gap $\Delta = 14.5$ GHz.

APPENDIX G: DEVICE 2 DRIVE-POWER DEPENDENCE

Figure 8 depicts additional measurements of device 2 at the same gate-voltage configuration as Fig. 4(a), $V_g = -0.7990$ V. The amplitude R of the resonator transmission S_{21} is shown as a function of the offset readout frequency $f_r - f_0$ and the phase difference across the junction φ in

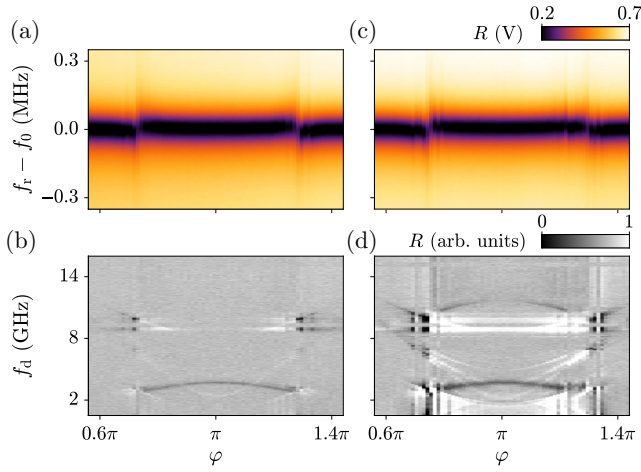


FIG. 8. (a) Device 2: amplitude R of the resonator transmission S_{21} as a function of offset readout frequency $f_r - f_0$ and phase φ , at the same gate voltage as Fig. 4(a), $V_g = -0.7990$ V, with $f_0 = 6.86731$ GHz. (b) Amplitude R of the resonator transmission S_{21} as a function of drive frequency f_d ($P_d = -35$ dBm) and phase φ , measured together with (a). Compared to Fig. 4(a), fewer transitions are visible in the spectrum. (c),(d) Same as (a),(b), but with $P_d = -25$ dBm. The same transitions as in Fig. 4(a) were observed.

Fig. 8(a). The resonator scans were acquired together with a two-tone spectroscopy measurement, shown in Fig. 8(b), for which the drive power was set to $P_d = -35$ dBm, lower than the drive power used for Fig. 4(a), $P_d = -28$ dBm. At this lower drive power, the PTs and the SQPT from E_1 to E_2 [Fig. 3(d) and green dashed line in Fig. 4(b)] are the most prominent transitions in the spectrum. This is expected for the PTs, with larger phase dispersion and therefore higher associated current, resulting in stronger coupling to the resonator in comparison to other transitions in the spectrum. Furthermore, the large linewidth and high intensity of the SQPT around $f_d = 4$ GHz in Fig. 4(a) indicate that this transition was also associated with larger current and thus coupled strongly to the resonator. For the two-tone spectroscopy measurement shown in Fig. 8(d), the drive power was increased to $P_d = -25$ dBm. Despite applying higher drive power, the same transitions were observed in Fig. 8(d) as in Fig. 4(a). The anticrossings observed in Fig. 8(c) deviate slightly from those in Fig. 8(a), even though the drive power was off during these measurements. We suspect that this phenomenon is associated with instabilities in the gate voltage or applied flux.

APPENDIX H: DEVICE 2 GATE DEPENDENCE

Figure 9(a) depicts the gate response of device 2, measured over a wide range of gate voltages at phase $\varphi = \pi$. As the gate voltage V_g was swept to more negative

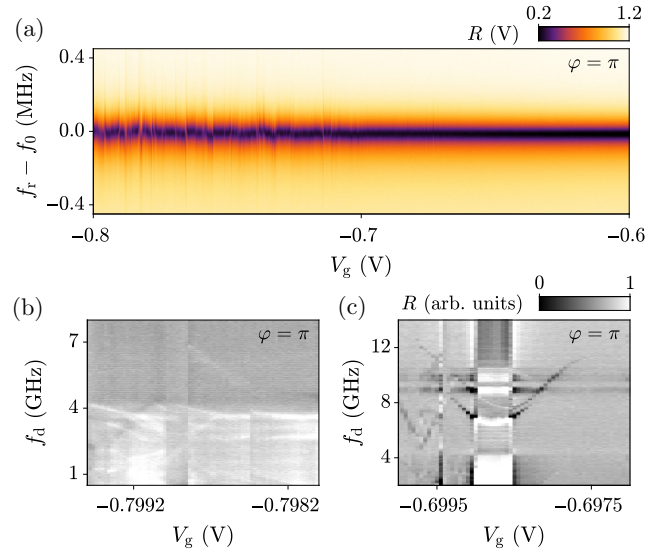


FIG. 9. (a) Device 2: amplitude R of the resonator transmission S_{21} as a function of offset readout frequency $f_r - f_0$ and gate voltage V_g . (b) Amplitude R of the resonator transmission S_{21} as a function of drive frequency f_d ($P_d = -35$ dBm) and gate voltage V_g , measured with 250 averages. (c) Same as (b), but for a different gate-voltage range and measured with $P_d = -30$ dBm and 500 averages. All measurements were performed at $\varphi = \pi$.

values, the resonator trace became less pronounced, indicative of a decrease in the internal quality factor, due to higher losses, which can be attributed to a larger current circulating in the superconducting loop of the device [17]. This larger current was paired with an increase in the number of ABSs in the junction, giving rise to more anticrossings in the left half of Fig. 9(a). The combination of many ABSs and gate-voltage-induced hysteresis caused gate-voltage instabilities in this device. Therefore, the two-tone spectroscopy measurements in Fig. 4 cannot be associated with specific values of the gate voltages V_g and V_s . Nonetheless, we present two gate-dependent two-tone spectroscopy measurements in Figs. 9(b) and 9(c), which were acquired at similar values of the gate voltage V_g as Figs. 4(a) and 4(c), respectively, with $V_s = 0$. Many dispersing ABS transitions were observed in these gate-voltage ranges, in agreement with the phase-dependence measurements. Instabilities in the gate voltage are evident in Fig. 9(b), where the spectrum seems to repeat itself below $V_g = -0.7985$ V.

- [1] A. F. Andreev, The thermal conductivity of the intermediate state in superconductors, *J. Exp. Theor. Phys.* **46**, 1823 (1964).
- [2] G. E. Blonder, M. Tinkham, and T. M. Klapwijk, Transition from metallic to tunneling regimes in superconducting microconstrictions: Excess current, charge imbalance, and supercurrent conversion, *Phys. Rev. B* **25**, 4515 (1982).

- [3] C. W. J. Beenakker, Universal limit of critical-current fluctuations in mesoscopic Josephson junctions, *Phys. Rev. Lett.* **67**, 3836 (1991).
- [4] A. Furusaki and M. Tsukada, Current-carrying states in Josephson junctions, *Phys. Rev. B* **43**, 10164 (1991).
- [5] J.-D. Pillet, P. Joyez, R. Žitko, and M. F. Goffman, Tunneling spectroscopy of a single quantum dot coupled to a superconductor: From Kondo ridge to Andreev bound states, *Phys. Rev. B* **88**, 045101 (2013).
- [6] F. Nichele, E. Portolés, A. Fornieri, A. M. Whiticar, A. C. C. Drachmann, S. Gronin, T. Wang, G. C. Gardner, C. Thomas, A. T. Hatke, M. J. Manfra, and C. M. Marcus, Relating Andreev bound states and supercurrents in hybrid Josephson junctions, *Phys. Rev. Lett.* **124**, 226801 (2020).
- [7] M. Coraiola, D. Z. Haxell, D. Sabonis, H. Weisbrich, A. E. Svetogorov, M. Hinderling, S. C. ten Kate, E. Cheah, F. Krizek, R. Schott, W. Wegscheider, J. C. Cuevas, W. Belzig, and F. Nichele, Phase-engineering the Andreev band structure of a three-terminal Josephson junction, *Nat. Commun.* **14**, 6784 (2023).
- [8] C. Janvier, L. Tosi, L. Bretheau, Ç. Ö. Girit, M. Stern, P. Bertet, P. Joyez, D. Vion, D. Esteve, M. F. Goffman, H. Pothier, and C. Urbina, Coherent manipulation of Andreev states in superconducting atomic contacts, *Science* **349**, 1199 (2015).
- [9] M. Hays, G. de Lange, K. Serniak, D. J. van Woerkom, D. Bouman, P. Krogstrup, J. Nygård, A. Geresdi, and M. H. Devoret, Direct microwave measurement of Andreev-bound-state dynamics in a semiconductor-nanowire Josephson junction, *Phys. Rev. Lett.* **121**, 047001 (2018).
- [10] L. Tosi, C. Metzger, M. F. Goffman, C. Urbina, H. Pothier, S. Park, A. L. Yeyati, J. Nygård, and P. Krogstrup, Spin-orbit splitting of Andreev states revealed by microwave spectroscopy, *Phys. Rev. X* **9**, 011010 (2019).
- [11] M. Hays, V. Fatemi, K. Serniak, D. Bouman, S. Diamond, G. de Lange, P. Krogstrup, J. Nygård, A. Geresdi, and M. H. Devoret, Continuous monitoring of a trapped superconducting spin, *Nat. Phys.* **16**, 1103 (2020).
- [12] M. Hays, V. Fatemi, D. Bouman, J. Cerrillo, S. Diamond, K. Serniak, T. Connolly, P. Krogstrup, J. Nygaard, A. Levy Yeyati *et al.*, Coherent manipulation of an Andreev spin qubit, *Science* **373**, 430 (2021).
- [13] V. Chidambaram, A. Kringhøj, L. Casparis, F. Kuemmeth, T. Wang, C. Thomas, S. Gronin, Geoffrey C. Gardner, Z. Cui, C. Liu, K. Moors, Michael J. Manfra, Karl D. Petersson, and Malcolm R. Connolly, Microwave sensing of Andreev bound states in a gate-defined superconducting quantum point contact, *Phys. Rev. Res.* **4**, 023170 (2022).
- [14] F. J. Matute-Cañadas, C. Metzger, S. Park, L. Tosi, P. Krogstrup, J. Nygård, M. F. Goffman, C. Urbina, H. Pothier, and A. L. Yeyati, Signatures of interactions in the Andreev spectrum of nanowire Josephson junctions, *Phys. Rev. Lett.* **128**, 197702 (2022).
- [15] P. Zellekens, R. S. Deacon, P. Perla, D. Grützmacher, M. I. Lepsa, T. Schäpers, and K. Ishibashi, Microwave spectroscopy of Andreev states in InAs nanowire-based hybrid junctions using a flip-chip layout, *Commun. Phys.* **5**, 267 (2022).
- [16] V. Fatemi, P. D. Kurilovich, M. Hays, D. Bouman, T. Connolly, S. Diamond, N. E. Frattini, V. D. Kurilovich, P. Krogstrup, J. Nygård, A. Geresdi, L. I. Glazman, and M. H. Devoret, Microwave susceptibility observation of interacting many-body Andreev states, *Phys. Rev. Lett.* **129**, 227701 (2022).
- [17] M. Hinderling, D. Sabonis, S. Paredes, D. Z. Haxell, M. Coraiola, S. C. ten Kate, E. Cheah, F. Krizek, R. Schott, W. Wegscheider, and F. Nichele, Flip-chip-based microwave spectroscopy of Andreev bound states in a planar Josephson junction, *Phys. Rev. Appl.* **19**, 054026 (2023).
- [18] J. J. Wesdorp, F. J. Matute-Cañadas, A. Vaartjes, L. Grünhaupt, T. Laeven, S. Roelofs, L. J. Splitthoff, M. Pita-Vidal, A. Bargerbos, D. J. van Woerkom, P. Krogstrup, L. P. Kouwenhoven, C. K. Andersen, A. L. Yeyati, B. van Heck, and G. de Lange, Microwave spectroscopy of interacting Andreev spins, *Phys. Rev. B* **109**, 045302 (2024).
- [19] M. Hinderling, S. C. ten Kate, M. Coraiola, D. Z. Haxell, M. Stiefel, M. Mergenthaler, S. Paredes, S. W. Bedell, D. Sabonis, and F. Nichele, Direct microwave spectroscopy of Andreev bound states in planar Ge Josephson junctions, *PRX Quantum* **5**, 030357 (2024).
- [20] B. H. Elfeky, K. Dindial, David S. Brandão, B. Pekerten, J. Lee, William M. Strickland, Patrick J. Strohhorn, A. Danilenko, L. Baker, M. Mikalsen, W. Schiela, Z. Liang, J. Issokson, I. Levy, I. Žutić, and J. Shabani, Microwave Andreev bound state spectroscopy in a semiconductor-based planar Josephson junction, *Phys. Rev. Res.* **7**, 013248 (2025).
- [21] Pavel D. Kurilovich, Vladislav D. Kurilovich, V. Fatemi, Michel H. Devoret, and Leonid I. Glazman, Microwave response of an Andreev bound state, *Phys. Rev. B* **104**, 174517 (2021).
- [22] Pavel D. Kurilovich, Vladislav D. Kurilovich, Aleksandr E. Svetogorov, W. Belzig, Michel H. Devoret, and Leonid I. Glazman, On-demand population of Andreev levels by their ionization in the presence of Coulomb blockade, *Phys. Rev. B* **110**, 184508 (2024).
- [23] A. Tosato, V. Levajac, J.-Y. Wang, C. J. Boor, F. Borsoi, M. Botifoll, C. N. Borja, S. Martí-Sánchez, J. Arbiol, A. Sammak, M. Veldhorst, and G. Scappucci, Hard superconducting gap in germanium, *Commun. Mater.* **4**, 23 (2023).
- [24] M. Lodari, A. Tosato, D. Sabbagh, M. A. Schubert, G. Capellini, A. Sammak, M. Veldhorst, and G. Scappucci, Light effective hole mass in undoped Ge/SiGe quantum wells, *Phys. Rev. B* **100**, 041304(R) (2019).
- [25] G. Scappucci, C. Kloeffer, F. A. Zwanenburg, D. Loss, M. Myronov, J.-J. Zhang, S. De Franceschi, G. Katsaros, and M. Veldhorst, The germanium quantum information route, *Nat. Rev. Mater.* **6**, 926 (2021).
- [26] L. Lakic, W. I. L. Lawrie, D. van Driel, L. E. A. Stehouwer, Y. Su, M. Veldhorst, G. Scappucci, F. Kuemmeth, and A. Chatterjee, A quantum dot in germanium proximitized by a superconductor, *Nat. Mater.* **24**, 552 (2025).
- [27] M. Hinderling, S. C. Ten Kate, D. Z. Haxell, M. Coraiola, S. Paredes, E. Cheah, F. Krizek, R. Schott, W. Wegscheider, D. Sabonis, and F. Nichele, Flip-chip-based fast inductive parity readout of a planar superconducting island, *PRX Quantum* **5**, 030337 (2024).

- [28] S. Probst, F. B. Song, P. A. Bushev, A. V. Ustinov, and M. Weides, Efficient and robust analysis of complex scattering data under noise in microwave resonators, *Rev. Sci. Instrum.* **86**, 024706 (2015).
- [29] S. W. Bedell, S. Hart, S. Bangsaruntip, C. Durfee, J. A. Ott, M. Hopstaken, M. S. Carroll, and P. Gumann, (Invited) Low-temperature growth of strained germanium quantum wells for high mobility applications, *ECS Trans.* **98**, 215 (2020).
- [30] J. Bardeen, L. N. Cooper, and J. R. Schrieffer, Theory of superconductivity, *Phys. Rev.* **108**, 1175 (1957).
- [31] M. Watanabe, K. Inomata, T. Yamamoto, and J. S. Tsai, Power-dependent internal loss in Josephson bifurcation amplifiers, *Phys. Rev. B* **80**, 174502 (2009).
- [32] G. Romero, I. Lizuain, V. S. Shumeiko, E. Solano, and F. S. Bergeret, Circuit quantum electrodynamics with a superconducting quantum point contact, *Phys. Rev. B* **85**, 180506(R) (2012).
- [33] S. Park, C. Metzger, L. Tosi, M. F. Goffman, C. Urbina, H. Pothier, and A. L. Yeyati, From adiabatic to dispersive readout of quantum circuits, *Phys. Rev. Lett.* **125**, 077701 (2020).
- [34] C. Metzger, S. Park, L. Tosi, C. Janvier, A. A. Reynoso, M. F. Goffman, C. Urbina, A. Levy Yeyati, and H. Pothier, Circuit-QED with phase-biased Josephson weak links, *Phys. Rev. Res.* **3**, 013036 (2021).
- [35] R. Haller, G. Fülöp, D. Indolese, J. Ridderbos, R. Kraft, L. Y. Cheung, J. H. Ungerer, K. Watanabe, T. Taniguchi, D. Beckmann, R. Danneau, P. Virtanen, and C. Schönenberger, Phase-dependent microwave response of a graphene Josephson junction, *Phys. Rev. Res.* **4**, 013198 (2022).
- [36] Philip F. Bagwell, Suppression of the Josephson current through a narrow, mesoscopic, semiconductor channel by a single impurity, *Phys. Rev. B* **46**, 12573 (1992).
- [37] M. R. Sahu, F. J. Matute-Cañadas, M. Benito, P. Krogstrup, J. Nygård, M. F. Goffman, C. Urbina, A. L. Yeyati, and H. Pothier, Ground-state phase diagram and parity-flipping microwave transitions in a gate-tunable Josephson junction, *Phys. Rev. B* **109**, 134506 (2024).
- [38] L. Massai, B. Hetényi, M. Mergenthaler, F. J. Schupp, L. Sommer, S. Paredes, S. W. Bedell, P. Harvey-Collard, G. Salis, A. Fuhrer, and N. W. Hendrickx, Impact of interface traps on charge noise and low-density transport properties in Ge/SiGe heterostructures, *Commun. Mater.* **5**, 151 (2024).
- [39] S. Park and A. L. Yeyati, Andreev spin qubits in multichannel Rashba nanowires, *Phys. Rev. B* **96**, 125416 (2017).
- [40] S. Bosco, M. Benito, C. Adelsberger, and D. Loss, Squeezed hole spin qubits in Ge quantum dots with ultrafast gates at low power, *Phys. Rev. B* **104**, 115425 (2021).
- [41] C. Adelsberger, S. Bosco, J. Klinovaja, and D. Loss, Enhanced orbital magnetic field effects in Ge hole nanowires, *Phys. Rev. B* **106**, 235408 (2022).
- [42] S. Hoffman and C. Tahan, Resolving Andreev spin qubits in germanium-based Josephson junctions, *ArXiv:2506.13988*.
- [43] M. Luethi, K. Laubscher, S. Bosco, D. Loss, and J. Klinovaja, Planar Josephson junctions in germanium: Effect of cubic spin-orbit interaction, *Phys. Rev. B* **107**, 035435 (2023).
- [44] D. Costa, P. D. Vecchio, K. Hudson, L. E. A. Stehouwer, A. Tosato, D. D. Esposti, M. Lodari, S. Bosco, and G. Scappucci, Buried unstrained germanium channels: A lattice-matched platform for quantum technology, *ArXiv:2506.04724*.
- [45] O. O. Shvetsov, A. Khola, V. Buccheri, I. P. C. Cools, N. Trnjanin, A. Geresdi, T. Kanne, and J. Nygård, Approaching the ultrastrong-coupling regime between an Andreev level and a microwave resonator, *Phys. Rev. Appl.* **24**, 044015 (2025).
- [46] <https://doi.org/10.5281/zenodo.17580733>.